Random close packing of disks and spheres in confined geometries

Kenneth W. Desmond and Eric R. Weeks
Department of Physics, Emory University, Atlanta, Georgia 30322, USA
(Received 3 March 2009; revised manuscript received 22 July 2009; published 30 November 2009)

Studies of random close packing of spheres have advanced our knowledge about the structure of systems such as liquids, glasses, emulsions, granular media, and amorphous solids. In confined geometries, the structural properties of random-packed systems will change. To understand these changes, we study random close packing in finite-sized confined systems, in both two and three dimensions. Each packing consists of a 50-50 binary mixture with particle size ratio of 1.4. The presence of confining walls significantly lowers the overall maximum area fraction (or volume fraction in three dimensions). A simple model is presented, which quantifies the reduction in packing due to wall-induced structure. This wall-induced structure decays rapidly away from the wall, with characteristic length scales comparable to the small particle diameter.

DOI: 10.1103/PhysRevE.80.051305 PACS number(s): 45.70.−n, 61.20.−p, 64.70.kj

I. INTRODUCTION

Random close packing (rcp) has received considerable scientific interest for nearly a century dating back to the work of Westman in 1930 [1–6] primarily due to the relevance rcp has to a wide range of problems, including the structure of living cells [7], liquids [8,9], granular media [10–13], emulsions [14], glasses [15], amorphous solids [16], jamming [17], and the processing of ceramic materials [18]. Typically, one defines rcp as a collection of particles randomly packed into the densest possible configuration. More rigorous definitions are available [7], but it is generally accepted that the rcp density of a packing of spheres is $\phi_{\mathrm{rcp}} \approx 0.64$. Packings can have other rcp densities when the particles are polydisperse mixture of spheres [19–24], nonspherical in shape [25–29], or confined within a container that is comparable in size to a characteristic particle size [18,30–39].

While most studies of rcp focus on infinite systems, real systems have boundaries and often these boundaries are important as highlighted by Carman in 1937 [30]. In the experiments by Carman, the packing fraction dependence on container size was measured for spheres poured into a cylindrical container and shaken for sufficiently long enough time to reach a very dense state. It was found that the packing fraction decreases with container size, which was attributed to the boundaries, altering the structure of the packing in the vicinity of the wall.

Since the work of Carman, there have been many other studies, which have investigated rcp in confined systems [6,35,40,41]. These studies have shown that near the boundary, particles tend to pack into layers, giving rise to a fluctuating local porosity with distance from the wall, ultimately affecting the macroscopic properties of highly confined systems. Other studies have examined the packing of granular particles in narrow silos, focusing on the influence of confinement on stresses between particles and the wall [42–45]. Nearly all of these studies did not directly measure the local packing or any local packing parameters with relation to distance from the side wall, with the exception of a few experiments that used x-ray imaging to view the structure of confined packings. In these experiments, the packings were monodisperse, facilitating highly ordered packing near the boundary, with measurements carried out at only a few different container size to particle size ratios [37,41].

Even with the history of work on the study of rcp in confined geometries, there is little known about how sensitive the structure of the packing near the boundary is to small changes in the confining width. For example, prior work found nonmonotonic dependence of ϕ_{rcp} on container size but only at extremely small containers with narrow dimensions h only slightly larger than the particle diameter d, that is, $h \approx 3d$ or smaller [30,36,38]. However, their data were not strong enough to look for such effects at larger container sizes. Additionally, primarily only confined monodisperse systems have received much attention, and these systems are susceptible to crystallization near flat walls, which greatly modify the behavior [46]. (One group did study binary systems, but they were unable to directly observe the structure [35].) Furthermore, two-dimensional (2D) confined systems have not been studied systematically, although they are relevant for a wide range of granular experiments [47].

In this paper, we address these questions using computer-simulated rcp packings in confined geometries. In particular, we study binary mixtures to prevent wall-induced crystallization [48–50]. We create 2D and three-dimensional (3D) packings with flat confining walls. In some cases, the system is confined only along one dimension (with periodic boundaries in the other directions), and in other cases we confine the sample along all directions. Our simulations are carried out at many different and very closely spaced confining thicknesses, spanning a large range of values to elucidate the effects small changes in confining thickness has on the structure.

We find that confinement significantly modifies the rcp states, with lowered values for ϕ_{rcp}, reflecting an inefficient packing near the walls. This inefficient packing persists several particle diameters away from the wall, although its dominant effects are only within 1 to 2 diameters. The behavior of ϕ_{rcp} is not monotonic with increasing sample thickness, reflecting the presence of boundary layers near the walls.

Understanding the character of random close packing in confined geometries may be relevant for non-close-packed confined situations [51]. For example, when a liquid is con-

fined, its structure is dramatically changed; particles form layers near the wall, which ultimately affects the properties of the liquid [52–57]. The shearing of confined dense colloidal suspensions shows the emergence of new structures not seen before [58]. The flow of granular media through hoppers [59,60] or suspensions through constricted microfluidic and nanofluidic devices [61–64] can jam and clog, costing time and money.

One of our own motivations for this work was to help us understand prior experiments by our group, which studied the confinement of colloidal particles [65]. A dense suspension of colloidal particles behaves similarly to a glass [66]. For traditional glass formers, many experiments have studied how confinement modifies the glass transition; samples, which have a well-characterized glass transition in large samples, show markedly different properties when confined to small samples [50,51,67–72]. In our experimental work, the colloidal particles had much slower diffusion rates when confined between two parallel walls [65]. However, the experiments were difficult and we only examined behavior of a dense suspension at a few specific thicknesses. As noted above, in this current work we investigate how particles pack for a finely spaced set of thicknesses, to look for nonmonotonic behavior of the packing that might have been missed in the experiment. A second related question is whether confinement effects on glassy behavior are due to boundary effects or finite-size effects [73]. Our results show that boundaries significantly modify the packing, which may in turn modify the behavior of these confined molecular systems [51].

The paper is organized as follows. Section II outlines the algorithm we use to generate confined rcp states. Section III shows how the total packing fraction, particle number density, and local order of confined rcp states change with confining thickness and distance from the confining boundary. Finally, Sec. IV provides a simple model that predicts the packing fraction dependence with confinement.

II. METHOD

Our aim is to quantify how a confining boundary alters the structure of rcp disks in 2D and spheres in 3D and, in particular, to study how this depends on the narrowest dimension. This section presents our algorithm for 2D packings first and then briefly discusses differences for the 3D algorithm.

In 2D, our system consists of a binary mixture of disks containing an equal number $N/2$ large disks of diameter d_l and small disks of diameter d_s with size ratio $\sigma=d_l/d_s=1.4$. For each configuration, disks are packed into a box of dimensions L_x by L_y. For most simulations we discuss, there is a periodic boundary condition along the x direction and two fixed hard boundaries (walls) along the y direction; although as discussed below, in some cases we consider periodic boundaries in all directions or fixed boundaries in all directions.

Each configuration is generated using a method adapted from Xu *et al.* [74], which is an extension of a method proposed by Clarke and Wiley [75]. This method is briefly summarized in Fig. 1. Infinitesimal particles are placed at random [76] in the system, gradually expanded and moved at each step to prevent particles from overlapping. When a final state is found such that particles can no longer be expanded without necessitating overlap, the algorithm terminates. Near the conclusion of the algorithm, we alternate between expansion and contraction steps to accurately determine the state.

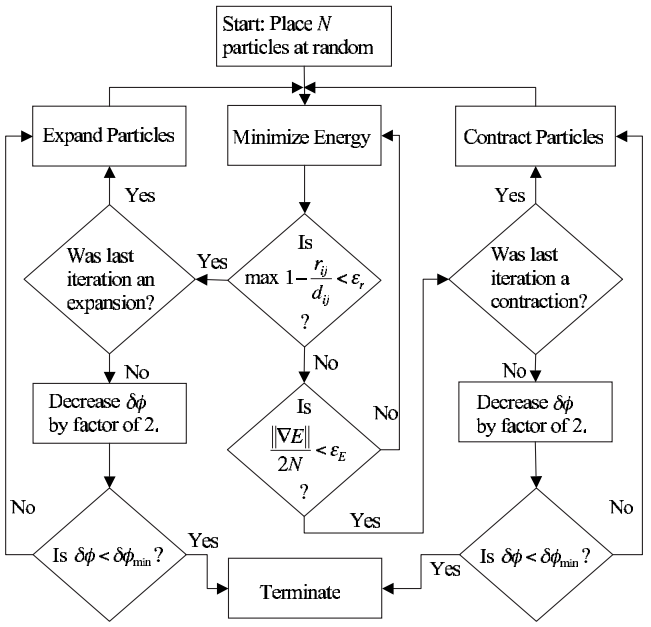

FIG. 1. A flow chart outlining our algorithm for computing rcp configurations.

In particular, while the final state found is consistent with hard particles (no overlaps allowed), the algorithm uses a soft potential at intermediate steps [74], given by

$$V(r_{ij}) = \frac{\epsilon}{2}(1 - r_{ij}/d_{ij})2\Theta(1 - r_{ij}/d_{ij}), \tag{1}$$

where r_{ij} is the center to center distance between two disk i and j, ϵ is a characteristic energy scale ($\epsilon=1$ for our simulations), $d_{ij}=(d_i+d_j)/2$, and $\Theta(1-r_{ij}/d_{ij})$ is the Heaviside function, making V nonzero for $r_{ij}<d_{ij}$. Simulations begin by randomly placing disks within a box of desired dimensions and boundary conditions with the initial diameters chosen such that $\phi_{initial} \ll \phi_{\mathrm{rcp}}$. In the initial state, particles do not overlap and the total energy $E=0$.

Next, all disk diameters are slowly expanded subject to the fixed size ratio $\sigma=1.4$ and ϕ changing by $\delta\phi$ per iteration; we start with $\delta\phi=10^{-3}$. After each expansion step, we check if any disks overlap by checking the condition $1-r_{ij}/d_{ij} > \epsilon_r=10^{-5}$ for each particle pair. Below this limit, we assume the overlap is negligible. If any particles do overlap ($E>0$), we use the nonlinear conjugate gradient method [77] to decrease the total energy by adjusting the position of disks so they no longer overlap ($E=0$). In practice, one energy minimization step does not guarantee that we have reached a minimum within the desired numerical precision. Thus, this step can be repeated to further reduce the energy if $E>0$. We judge that we have reached a nonzero local mini-

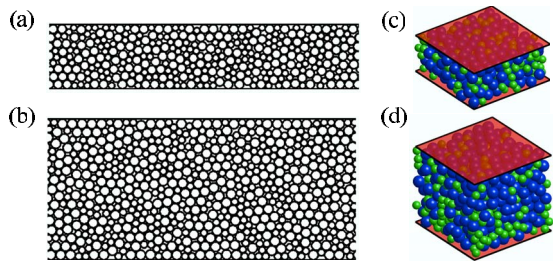

FIG. 2. (Color online) Illustrations of 2D and 3D configurations generated using the algorithm described in Sec. II. (a) 2D configuration for $h=10$. (b) 2D configuration with $h=20$. (c) 3D configuration with $h=5$, where blue (dark gray) represents big particles and green (light gray) represents small particles. (d) 3D configuration with $h=10$.

mum if the condition $\|\nabla E\|/(2N) < \epsilon_E = 10^{-7}$ is found, where $\|\nabla E\|$ is the magnitude of the gradient of E. Physically speaking, this is the average force per particle, and the threshold value (10^{-7}) leads to consistent results.

If we have such a state with $E>0$, this is not an rcp state as particles overlap. Thus, we switch and now slowly contract the particles until we find a state where particles again no longer overlap (within the allowed tolerance). At that point, we once again begin expansion. Each time we switch between expansion and contraction, we decrease $\delta\phi$ by a factor of 2. Thus, these alternating cycles allow us to find an rcp state of nonoverlapping particles (within the specified tolerance) and determine ϕ_{rcp} to high accuracy. We terminate our algorithm when $\delta\phi < \delta\phi_{\mathrm{min}} = 10^{-6}$. In practice, we have tested a variety of values for the thresholds ϵ_r, ϵ_E, and $\delta\phi_{\mathrm{min}}$ and find that our values guarantee reproducible results as well as reasonably fast computations. Our algorithm gives an average packing fraction of $\phi_{\mathrm{rcp}} = 0.8420 \pm 0.0005$ for 40 simulated rcp states, containing 10 000 particles with periodic boundary conditions along both directions. Our value of ϕ_{rcp} is in agreement with that found by Xu *et al.* [74].

The above procedure is essentially the same as Ref. [74]; we modify this to include the influence of the boundaries. To add in the wall, we create image particles reflected about the position of the wall; thus, particles interact with the wall using the same potential [Eq. (1)].

Additionally, we wish to generate packings with prespecified values for the final confining height $h=L_y/d_s$. (This allows us to create multiple rcp configurations with the same h.) We impose h by affinely scaling the system after each step, so that the upper boundary is adjusted by $L_y = h d_s$ and each disk's y coordinate is multiplied by the ratio $L_{y,i+1}/L_{y,i}$, where $L_{y,i}$ and $L_{y,i+1}$ are the confining widths between two consecutive iterations. Thus, while d_s gradually increases over the course of the simulation, L_y increases proportionally so that the nondimensional ratio h is specified and constant. Some examples of our final rcp states are shown in Fig. 2.

To ensure we will have no finite-size effects in the periodic direction, we examined ϕ_{rcp} for different h and L_x and found $\phi_{\mathrm{rcp}}(h)$ to be independent of L_x for $3 \leq h \leq 30$ if $L_x/d_s > 40$. Thus, we have chosen N for each simulation to guarantee $L_x/d_s \approx 50$.

In 3D, our system consists of a binary mixture of spheres, containing an equal number $N/2$ large spheres of diameter d_l and small spheres of diameter d_s with a size ratio $\sigma = d_l/d_s = 1.4$. Spheres are packed into a box of dimensions L_x by L_y by L_z, with periodic boundaries along the x and z directions and a fixed hard boundary along the y direction. Each configuration is generated using the same particle expansion and contraction method described above and the same initial values for $\delta\phi$ and the terminating conditions. For each configuration $L_x = L_z$, $h = L_y/d_s$, and N is chosen so that $L_x/d_s > 10$. Our choice of $L_x/d_s > 10$ is not large enough to avoid finite effects. However, in order to acquire the large amount of data needed in a reasonable amount of time, we intentionally choose a value of L_x/d_s below the finite-size threshold. Trends observed in the 2D analysis will be used to support that any similar trends seen in 3D are real and not the result of the finite periodic dimensions. Note that in 3D we will show cases where $h > L_x/d_s$, resulting in the confining direction being larger than the periodic direction, and this may affect the structure of final configurations; however, we will not draw significant conclusions from those data.

Overall, it is not known if this algorithm produces mathematically rigorously defined random close-packed states [7,17,74,78]. However, the goal of this paper is to determine empirically the properties of close-packed states in confinement, and we are not attempting to extract mathematically rigorous results. For example, we are not as interested in the specific numerical values of ϕ_{rcp} that we obtain, but rather the qualitative dependence on h. As noted in the introduction, different computational and experimental methods for creating rcp systems have different outcomes, and so it is our qualitative results we expect will have the most relevance.

Note that for the remainder of this paper, we will drop the subscript rcp, and it should be understood that discussions of ϕ refer to the final state found in each simulation run $\phi_{\mathrm{rcp}}(h)$.

III. RESULTS

A. 2D systems

We begin by generating many 2D configurations with h between 3-30 and computing the packing fraction for each, as shown by the black curve in Fig. 3. This plot shows that confinement lowers ϕ, with the influence of the walls being increasingly important at lower h. The lowering of ϕ with confinement is most likely due to structural changes in the packing near the confining boundary. We know that any alteration in particle structure from a rcp state must be "near" the wall because as $h \to \infty$, we expect to recover a packing fraction of ϕ_{rcp}, implying that in the infinite system the "middle" of the sample is composed of an rcp region. Extrapolating the data in Fig. 3 to $h \to \infty$, we find $\phi_{h\to\infty} = \phi_{\mathrm{rcp}} = 0.842$, which is essentially a test of our method. The extrapolation (red curve in Fig. 3) was carried out by assuming that to first order $\phi \sim \phi_{h\to\infty} - C/h$ for large h, where $\phi_{h\to\infty} = \phi_{\mathrm{rcp}}$ (the bulk value for the rcp packing) and C is a fitting parameter.

The data in Fig. 3 begin to deviate from the fit for $h \lesssim 6$ and, furthermore, $\phi(h)$ is not monotonic. While some of the variability is simply noise due to the finite number of disks N used in each simulation, some of the variability is real. The inset in Fig. 3 shows a magnified view of the region

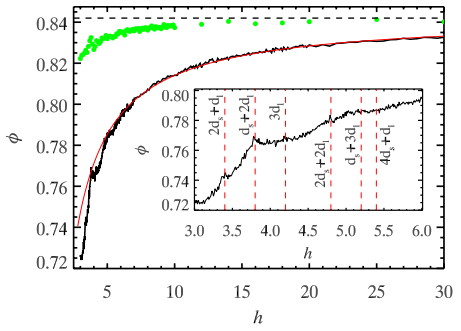

FIG. 3. (Color online) The black curve is the average packing fraction ϕ found by averaging at least ten 2D configurations together for various confining widths h; recall that h has been nondimensionalized by d_s, the small particle diameter. The smooth red curve (dark gray) is a fit using Eq. (5), which finds $\phi_{\mathrm{rcp}}=0.842$ in the limit $h\to\infty$; the value for ϕ_{rcp} is indicated by the black dashed line. The green (light gray) data points are $\phi(h)$ computed for many configurations with the confining wall replaced by a periodic boundary. The inset is a magnified view of the region for $h\leq 6$ to better show the large variations within this range. The vertical lines in the inset are located at "special" h values, where peaks and plateaus appear.

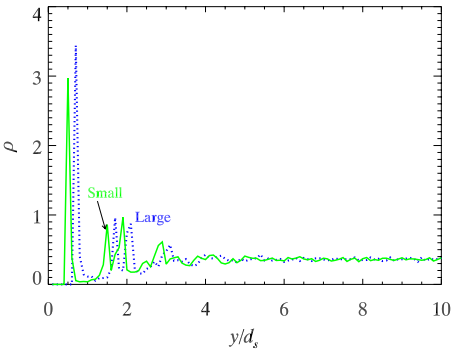

FIG. 4. (Color online) A plot of the number density $\rho(y)$ for 100 2D configurations at $h=30$ averaged together. The plot is constructed by treating the small and big particles separately and using bins along the confining direction of width $\delta y=0.1d_s$.

$3\leq h\leq 6$. The vertical lines in this inset are located at specific values of h that can be expressed as the integer sums of the two-particle diameters. For instance, the first vertical line near the y axis is located at $h=2d_s+d_l$. These lines are placed at some h values, where $\phi(h)$ has notable spikes or plateaus. These lines suggest that there exist special values of h, where the confining thickness is the right width so that particles can pack either much more efficiently or much less efficiently than nearby values of h. Intriguingly, these special h values do not appear to be as pronounced at all possible integer sums, but instead only the selected few are drawn in the figure. However, given the apparent noisy fluctuations (despite averaging over a very large number of simulations), we cannot completely rule out that local maxima and minima might also exist at other combinations of d_s and d_l. Somewhat surprisingly, we do not observe large peaks corresponding to integer combinations of $(\sqrt{3}/2)d_s$ or $(\sqrt{3}/s)d_l$, which would suggest hexagonal packing, the easiest packing of monodisperse disks in 2D; whereas, the observed peaks of $\phi(h)$ suggest squarelike packing.

To measure structural changes in particle packing as a result of confinement, we start by examining the variations in the local number density ρ with distance y from the confining wall. We define ρ to be the average number of particles per unit of area along the unconfined direction. For a given location y, we count the number of particles in a region of area $L_x\Delta y$ and divide by this area, choosing Δy to be of a size such that the results do not depend sensitively on the choice but also so that we can get reasonably localized information. Figure 4 is a plot of $\rho(y)$ for 100 configurations averaged together at $h=30$. This plot shows oscillations in particle density, which decay to a plateau. The oscillations near the wall are indicative of particles layering in bands. Above $y\gtrsim 6d_s$, noise masks these oscillations. This supports our interpretation that confinement modifies the structure near the walls but not in the interior. Furthermore, the rapidity of the decay to the plateau seen in Fig. 4 suggests that confinement is only a slight perturbation to systems with overall size $h\gtrsim 6$.

The details of the density profiles in Fig. 4 also suggest how particles pack near the wall. The small particle density (solid line) has an initial peak at $y=0.5d_s$, indicating many small particles in contact with the wall, as their centers are one radius away from $y=0$. Likewise, the large particle density (dashed line) has its initial peak at $y=0.7d_s=0.5d_l$, indicating that those particles are also in contact with the wall. This is consistent with the pictures shown in Figs. 2(a) and 2(b), where it is clear that particles pack closely against the walls. Examining again the small particle number density in Fig. 4 (solid line), the secondary peaks occur at $y=1.5d_s$ and $y=1.9d_s=0.5d_s+1.0d_l$, which is to say either one small particle diameter or one large particle diameter further away from the first density peak at $y=0.5d_s$. This again is consistent with particles packing diameter to diameter rather than "nesting" into hexagonally packed regions. Similar results are seen for the large particles (dashed line), which have secondary peaks at $y=1.0d_s+0.5d_l$ and $y=2.1d_s=1.5d_l$.

To confirm that these density profile results apply for a variety of thicknesses h, and more importantly to see how these results are modified for very small h, we use an image representation shown in Fig. 5. To create this image, density distributions of different h are each separately rescaled to a maximum value of 1. Every data point within each distribution is then made into a grayscale pixel indicating its relative value; black is a relative value of 1, and white is a relative value of 0. The vertical axis is the confining width and the horizontal axis is the distance y from the bottom wall. Each horizontal slice (constant h) is essentially the same type of distribution shown in Fig. 4. The white space on the right side of Fig. 5 arises because the distribution is only plotted for the range $0\leq y\leq h/2$. The distributions are symmetric about $y=h/2$ and by averaging the distribution found for the range $0\leq y\leq h/2$ with the distribution found for the range $h/2\leq y\leq h$, the statistics are doubled. The areas shown in the insets are magnified views, where the full range $0\leq y\leq h$ is being shown.

In Fig. 5, there are vertical strips of dark areas, once again indicating that particles are forming layers. The width of

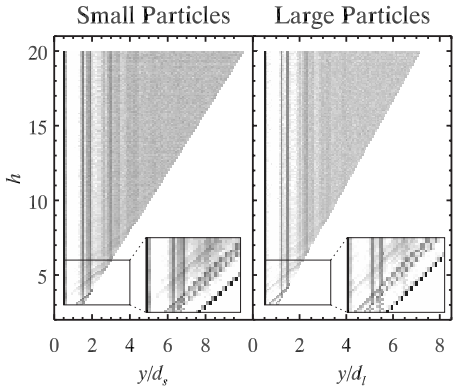

FIG. 5. An image representation constructed for the purpose of comparing 2D $\rho(y)$ distributions at many different h. The intensities have been logarithmically scaled. The vertical pixel width is 0.1 and for the left plot the horizontal pixel width is 0.2 and for the right plot the horizontal pixel width is 0.14.

these strips widens and the intensity lessens farther from the wall. In each plot, the first vertical black strip is sharply defined and located at one-particle radius, illustrating that small and big particles are in contact with the wall. Finally, the location and width of each layer remain essentially the same for different h, suggesting that layering arises from a constraint imposed by the closest boundary. Given that the first layer of particles always packs against the wall, this imposes a further constraint on how particles pack in the nearby vicinity. The consistency in the location and width of the second layer for all h demonstrates that the constraint of the first layer always produces a similar packing in the second layer, essentially independent of h. Continuing this argument, each layer imposes a weaker constraint on the formation of a successive layer, allowing for the local packing to approach rcp far from the wall.

In the magnified views of Fig. 5, the vertical dark lines show the layering of particles induced by the left boundary and the angled dark lines show the layering of particles induced by the right boundary. We see that for small h, these sets of lines overlap and intersect, meaning that there is a strong influence from one boundary on the packing within the layers produced by the other boundary. This may explain the variations seen in $\phi(h)$ for small h in Fig. 3. In particular, it is clear that at certain values of h, the layers due to one wall are coincident with the layers due to the other wall, and this suggests why $\phi(h)$ has a higher value for that particular h. Given that the layer spacings correspond to integer combinations of d_s and d_l, the coincidence of layers from both walls will correspond to integer combinations of d_s and d_l, and this thus gives insight into the peak positions shown in the inset of Fig. 3.

As described above, the influence of the walls diminishes rapidly with distance y away from the wall. In particular, for the local number density $\rho(y)$, we observe that the asymptotic limit $\rho(y\to\infty)=0.362$ for the curves shown in Fig. 4 is in agreement with the theoretical number density of an rcp configuration $\rho_{\mathrm{rcp}}=4\phi_{\mathrm{rcp}}/\pi(1+\sigma)$. To quantify the approach to the asymptotic limit, we define a length scale from a spatially varying function $f(y)$ using

$$\lambda = \frac{\int y[f(y)-f(y\to\infty)]^2 dy}{\int [f(y)-f(y\to\infty)]^2 dy}. \tag{2}$$

In this equation, $f(y)$ is an arbitrary function, where the value of λ quantifies the weighting of $f(y)$. For simple exponential decay $f(y)=Ae^{(-y/\lambda')}$, Eq. (2) gives $\lambda=\lambda'/2$. Using $f(y)=\rho(y)$, we find $\lambda=0.85d_s$ and $\lambda=0.72d_s$ for the small particle curve and big particle curve in Fig. 4, respectively, suggesting that the transition from wall-influenced behavior to bulk rcp packing happens extremely rapidly.

To further investigate the convergence of the local packing to rcp more closely, we analyze the local bond order parameters ψ_n, which for a disk with center of mass r_i are defined as

$$\psi_n(r_i) = \frac{1}{n_b}\left|\sum_j e^{ni\theta(r_{ij})}\right|. \tag{3}$$

The sum is taken over all j particles that are neighbors of the ith particle, $\theta(r_{ij})$ is the angle between the bond connecting particles i and j and an arbitrary fixed reference axis, and n_b is the total number of i-j bonds [79]. (These are not physical bonds but indicate that two particles are nearest neighbors, where the definition of nearest neighbor is set by the first minimum of the pair-correlation function.) The magnitude of ψ_n^2 is bounded between zero and one; the closer the magnitude of ψ_n^2 is to 1, the closer the local arrangement of neighboring particles is to an ideal n-sided polygon. Figures 6(a)–6(c) are drawings illustrating the concept of ψ_n^2 using a 2D configuration with $h=10$. Particles with larger ψ_n^2 are drawn darker. These figures have no large clusters of dark colored particles, demonstrating that there are no large crystalline domains (i.e., particles are randomly packed).

For a highly ordered monodisperse packing, $\langle\psi_6^2\rangle$ would be the most appropriate choice for measuring order because of the ability for monodisperse packings to form hexagonal packing. However, for a bidisperse packing with size ratio $\sigma=1.4$, the average number of neighbors a small particle will have is 5.5 and the average number of neighbors big particles will have is 6.5. Therefore, a bidisperse packing of this kind will have a propensity to form local pentagonal, hexagonal, and heptagonal packing, and to properly investigate how the local packing varies we examine $\langle\psi_5^2\rangle$, $\langle\psi_6^2\rangle$, and $\langle\psi_7^2\rangle$. We compute the average values $\langle\psi_5^2\rangle$, $\langle\psi_6^2\rangle$, and $\langle\psi_7^2\rangle$ for all configurations, as a function of y, and averaging together all $\langle\psi_n^2\rangle$ distributions for configurations with $h\geq 16$ to improve statistics. This averaging can be justified by considering that oscillations in $\rho(y)$ in Fig. 4 for $y/d_s>10$ are quite small. Thus, this averaging improves our statistics for the range $0<y/d_s<5$, where the largest oscillations occur, without skewing the data. In the end, nearly 10 000 configurations are averaged together, producing the curves shown in Figs. 7(b)–7(d). This figure shows the spatial variations of $\langle\psi_5^2\rangle$, $\langle\psi_6^2\rangle$, and $\langle\psi_7^2\rangle$ for small and big particles separately and both particles combined. All curves show fluctuations that decay with distance from the wall and show local order within and

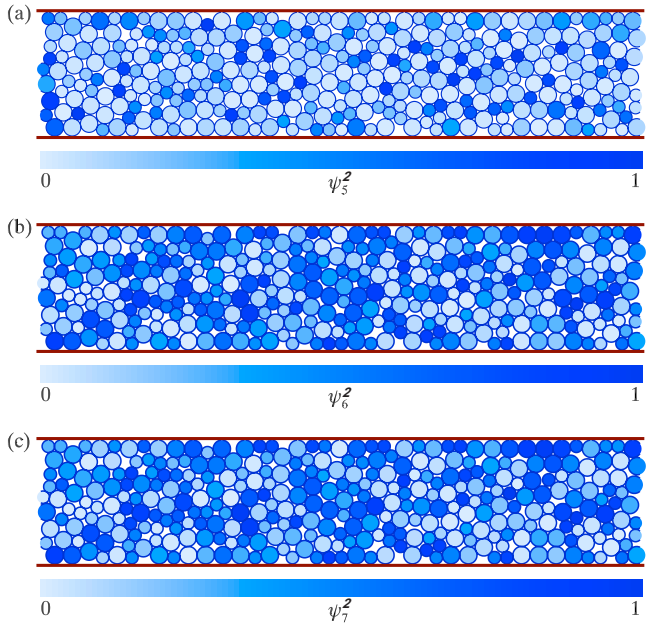

FIG. 6. (Color online) Drawings illustrating the conceptual meaning of (a) ψ_5^2, (b) ψ_6^2, and (c) ψ_7^2. Darker colored particles have neighbors that are packed more like an ideal regular n-sided polygon as compared to lighter drawn particles. The configuration of particles is the same for all panels and are drawn from a simulation with $h=10$. Note in (b) that there are no large patches of high ψ_6^2, demonstrating that there are no large crystalline domains.

between layers. Figure 7(a) has been added so comparisons between the locations of the oscillations in $\rho(y)$ and $\langle\psi_n^2\rangle(y)$ can be made.

Each successive layer has less orientational order than the previous layer with $\langle\psi_n^2\rangle$ eventually decaying to an asymptotic limit. To characterize a length scale for these curves, we compute λ using Eq. (2) for each curve shown in Figs. 7(b)–7(d). From the nine curves, we find that the mean value of $\lambda=(1.00\pm0.24)d_s$. The length scales found for these curves are once again less than the largest particle diameter. No striking difference is found between the different order parameters or between the different particle sizes; specific values of λ are given in the figure caption. (Note that the asymptotic limits of all $\langle\psi_n^2\rangle$ plots are in agreement with the average values found for 40 unconfined 10 000 particle simulations averaged together, confirming that the local packing converges to an rcp arrangement far from the walls.)

Next, we wish to distinguish the structural influence of the flat wall from the finite-size effects. We perform simulations, where the confining wall is replaced by a periodic boundary with periodicity h; thus, particles cannot form layers. In this case, the packing fraction still decreases as h is decreased, as shown by the green curve (light gray) in Fig. 3, although the effect is less striking than for the case with walls (black curve). A likely explanation for the decrease in ϕ with confinement is the long-range structural correlations imposed along the constricted direction; in other words, if there is a particle located at (x,y) that particle is mirrored at $(x,y-h)$ and $(x,y+h)$ by the periodic boundary. We know from the pair-correlation function [19,21] of rcp configurations that structural correlations exist over distances of many particle

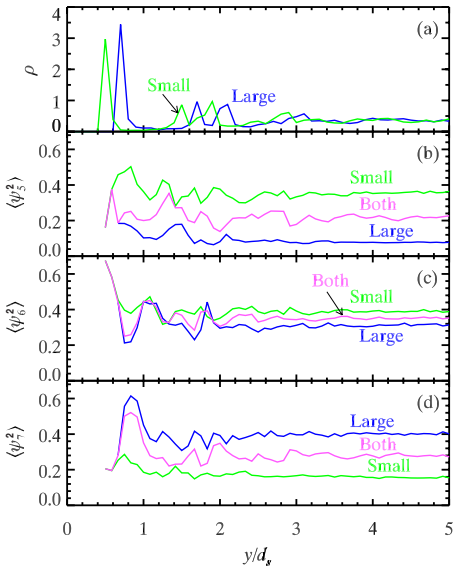

FIG. 7. (Color online) (a) A plot of the local number density $\rho(y)$ for 2D configurations of big and small particles separately. [(b)–(d)] Plots of $\langle\psi_n^2\rangle(y)$ for small (green/light gray) and big particles (blue/dark gray) separately and both sizes together (light purple/medium gray) where (b) is $\langle\psi_5^2\rangle$, (c) is $\langle\psi_6^2\rangle$, and (d) is $\langle\psi_7^2\rangle$. The length scales determined from these curves for small, large, and both species are $\lambda_{5,s}=1.2$, $\lambda_{5,l}=1.1$, $\lambda_{5,b}=1.4$, $\lambda_{6,s}=0.8$, $\lambda_{6,l}=0.9$, $\lambda_{6,b}=0.8$, $\lambda_{7,s}=1.1$, $\lambda_{7,l}=0.7$, and $\lambda_{7,b}=1.0$ (all in terms of d_s).

diameters, although of course these are weak at larger distances. Thus, the periodicity forces a deviation from the ideal rcp packing that becomes more significant as h decreases. By definition, rcp is the most random densely packed state and, thus, any perturbations away from this state must have a lower packing fractions. However, this is not nearly as significant as the constraint imposed by the flat wall, as is clear comparing the green (light gray) data and the black data in Fig. 3.

B. 3D systems

We next consider 3D confined systems. We start by investigating $\phi(h)$ shown as the black points in Fig. 8. As observed in the 2D case, ϕ is reduced as a result of confine-

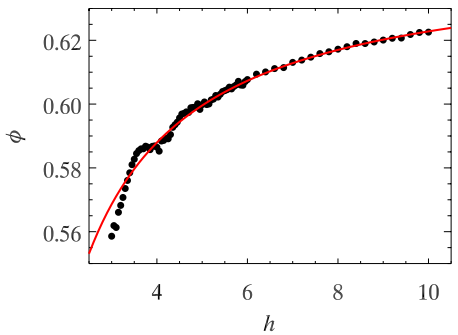

FIG. 8. (Color online) The black data points are the average packing fractions of 3D configurations at various h. The red (dark gray) curve is a fit to the model (5). For each h, at least ten configurations were averaged together.

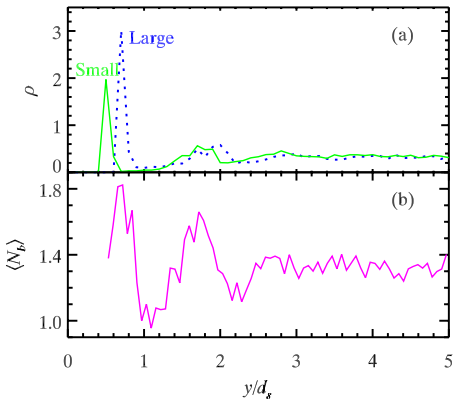

FIG. 9. (Color online) (a) A plot of $\rho(y)$ for 3D configurations for small and big particles separately. The plot is constructed using bins of width $\delta y=0.1d_s$ along the confining directions. (b) A plot of the average number of ordered bonds $\langle N_b\rangle(y)$.

ment. However, unlike the 2D system, there does not appear to be a series of "special values" of h that give rise to peaks and plateaus other than a hump near $h=3.75$. The lack of substructure may be due to the smaller size in x and z, in contrast with the 2D simulations, which had large sizes in the unconfined direction.

Next we investigate the local number density $\rho(y)$ (the average number of particles per unit area along the unconfined directions) for $h=25$ shown in Fig. 9(a). The data are constructed by averaging together 100 configurations. The curve shows fluctuations that decay with distance from the wall, eventually reaching a plateau. Using Eq. (2), we obtain decay lengths $\lambda_{3D}=0.77d_s$ and $0.73d_s$ for the small and large particle curves, respectively. These length scales are similar to the length scales obtained in the 2D case ($\lambda_{2D}=0.85d_s$ and $0.72d_s$ for small and large particles).

To compare all 3D $\rho(y)$ distributions for different h, we construct the image representation used to compare 2D configurations in Fig. 5. The data for the 3D configurations are shown in Fig. 10. Again there are dark vertical strips arising from particles forming layers near the wall. Like in 2D, the density approaches the "bulk" rcp value far from the wall.

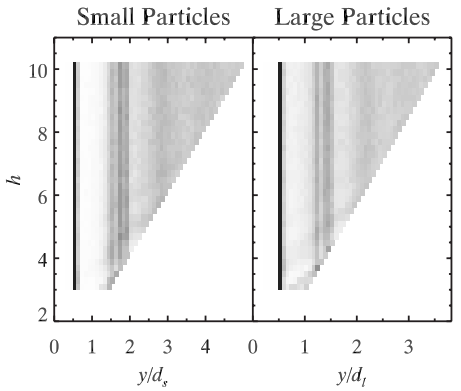

FIG. 10. An image representation comparing the number density distributions of 3D configurations for many different h. Black pixels represent a relative value of 1 and white represents a relative value of 0. A grayscale is used to represent relative values between 0 and 1. The pixel widths are $0.1d_s$ horizontally and 0.2 vertically.

In 2D, we also noted that the structure is modified near the wall, as measured by the ψ_n^2 order parameters. To investigate structural ordering in 3D, we use a local structural parameter sensitive to ordering [80,81]. We start by defining

$$\hat{q}_{i,6}=\frac{1}{n_j K}\sum_j Y_{6m}(\theta_{ij},\phi_{ij}). \tag{4}$$

In the above equation $m=\{-6,\ldots,0,\ldots,6\}$, and thus $\hat{q}_{i,6}$ is a 13 element complex vector, which is assigned to every particle i in the system. The sum in Eq. (4) is taken over the j nearest neighbors of the ith particle, n_j is the total number of neighbors, and K is a normalization constant so that $\hat{q}_{i,6}\cdot\hat{q}_{i,6}=1$. For two particles i and j that are nearest neighbors, $Y_{6m}(\theta_{ij},\phi_{ij})$ is the spherical harmonic associated with the vector pointing from particle i to particle j, using the angles θ_{ij} and ϕ_{ij} of this vector relative to a fixed axis. Next, any two particles m and n are considered "ordered neighbors" if $\hat{q}_{m,6}\cdot\hat{q}^*_{n,6}>0.5$ [80,81]. Finally, we quantify the local order within the system by the number of ordered neighbors N_b a particle has.

Figure 9(b) is a plot of the average number of ordered neighbors particles have $\langle N_b\rangle$ as a function of distance y from the wall. In comparison with Fig. 9(a), this plot shows that local order is mostly seen within layers not between layers. Also we see that $\langle N_b\rangle$ converges to an asymptotic value of ≈ 1.3, confirming that the system is disordered. (Values of $N_b\geq 8$ are considered crystalline [81].) We use Eq. (2) to characterize a length scale for the decay in $\langle N_b\rangle$, giving $\lambda=1.3d_s$. The asymptotic limit of $\langle N_b\rangle(y)$ in Fig. 9(b) agrees with the average value of N_b found for 15 large simulations with 2500 particles and periodic boundary conditions, confirming that the local structure in the confined case converges to the bulk rcp state far from the walls.

Our results show that in both 2D and 3D, confinement induces changes in structural quantities near the walls, with a decay toward the "bulk" values characterized by length scales no larger than d_l. The only prior work we are aware of with related results are a computational study [40] and an experimental study [41] of collections of monodisperse particles confined in a large silo. The simulation by Landry *et al.* primarily focused on the force network within the silo. They show one plot of the local packing fraction as a function of distance from the silo wall. Similar to our results, this local packing fraction showed fluctuations that decayed monotonically. In their paper, they state a decay length of $\approx 4d_l$; however, it appears that they drew this conclusion by estimating the value by eye. Applying Eq. (2) to their data, we find λ on the order of d_l, close to the value found in our simulations. The experimental study by Seidler *et al.* reported on the local bond orientational order parameter, which showed oscillation that decayed with distance from the wall. They reported a decay length of $\lambda\approx d_l$ using an exponential fit. The length scales from these two studies are slightly larger than those found in our work.

IV. MODEL

Our results for $\phi(h)$ can be understood with a simple model incorporating an effective boundary layer and a bulk-

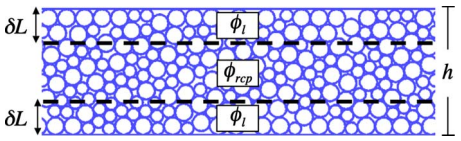

FIG. 11. (Color online) Illustration of the model for $\phi(h)$. The model breaks a configuration with confining width h into three regions. The boundary layers are approximated to have a packing fraction ϕ_l and persist a distance δL into the sample, and the middle bulk region is approximated to have a packing fraction ϕ_{rcp}. These three parameters are assumed to be h independent.

like region. This model is an extension of one proposed by Verman and Banerjee [31] and Brown and Hawsley in 1946 [32]. In Fig. 11, we show a configuration of particles confined between two plates and divided into two boundary layers and a bulk region. The model of Refs. [31,32] approximates the effect of the walls by assuming a lower effective volume fraction ϕ_l to the boundary layers. The central region is assumed to have a volume fraction ϕ_{rcp}, equal to the volume fraction for an infinite system. Of course, this model is an oversimplification that coarse grains the density near the walls, which in reality varies smoothly and nonmonotonically in space, as Sec. III demonstrates. Furthermore, this model will not capture the nonmonotonic behavior of Figs. 3 and 8, but it should capture the overall trend with h. In the original model of Refs. [31,32], it was conjectured that the thickness of the boundary layer is $\delta L=1d$ for monotonic particles of diameter d. The experimental data they tested the model with were too limited to carefully check this assumption; here, we extend their model by allowing δL to be a free parameter. (Clearly, our results, such as Fig. 7, confirm that $\delta L \approx 1 d_s$ is a reasonable order of magnitude.)

Using this simple model, ϕ can be approximated by the weighted average $\phi=\frac{h-2\delta L}{h}\phi_{\mathrm{rcp}}+\frac{2\delta L}{h}\phi_l$ (in either 2D or 3D, with different values of the parameters depending on the dimension). Reducing this equation further, we obtain

$$\phi = \phi_{\mathrm{rcp}} - \frac{C}{h}, \tag{5}$$

where we define the boundary packing parameter $C=2\delta L(\phi_{\mathrm{rcp}}-\phi_l)$, which quantifies how the wall influences the packing fraction near the boundary. Note that this is the same form for $\phi(h)$ obtained from considering a first-order correction in terms of $1/h$ and is the same empirical form assumed by Scott [5].

We investigate the merit of this model by fitting the data to Eq. (5), which only contains two fitting parameters ϕ_{rcp} and C. The data in both Figs. 3 and 8 are fitted to Eq. (5). The fits are shown as the red lines in these earlier figures and also in Fig. 12, where the data are plotted as functions of $1/h$ to better illustrate the success of this model. The fits give for 2D $\phi_{\mathrm{rcp}}=0.844$ and $C=0.317$ and for 3D $\phi_{\mathrm{rcp}}=0.646$ and $C=0.233$. Both fits give values for ϕ_{rcp} that are slightly larger, but not by much, than ϕ_{rcp} reported earlier in the paper. In Fig. 12, it can be seen that the packing fraction for large $1/h$ dips significantly below the fitting line, due to the fluctuations in $\phi(h)$ for small h; this is responsible for the

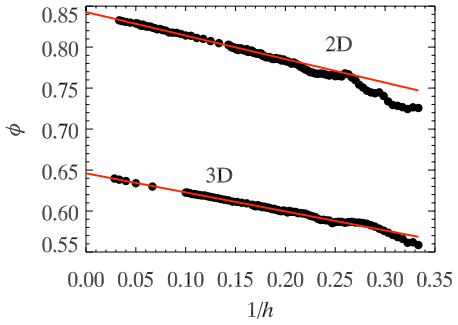

FIG. 12. (Color online) The upper black curve is a plot of $\phi(1/h)$ for 2D configurations and the red (dark gray) line going through the curve is a fit from the model [Eq. (5)]. Likewise, the lower black curve is a plot of $\phi(1/h)$ for 3D configurations with the red (dark gray) line going through the curve being another fit from the model.

overestimation on ϕ_{rcp}. When the data for both curves are fitted for $h \geq 8$ $(1/h<0.125)$, the actual values for ϕ_{rcp} are obtained. The dipping of the $\phi(h)$ curve below the line for large $1/h$ is perhaps due to the layering each wall produces affecting the layering produced by the opposite wall (see Figs. 5 and 10). Another possibility is that this reflects the breakdown of the model when $h \approx 2\delta L$. That is, when the thickness of the sample is such that the two boundary layers begin to overlap, the model would not be expected to work.

To provide further credence to the model, we also perform 2D rcp simulations with a fixed circular boundary or a fixed square boundary. Figure 13 shows a plot of $\phi(h)$ for both the circular boundary (green points) and the square boundary (blue points). In analogy with our prior results, h is the wall-to-wall distance: for the circular boundary, h is the diameter normalized by d_s, and for the square boundary h is the side length L normalized by d_s. As before with two parallel flat boundaries, we see that ϕ increases to an asymptotic limit.

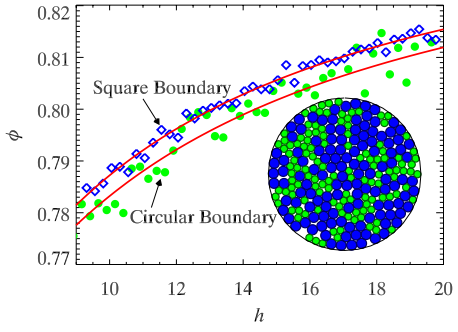

FIG. 13. (Color online) $\phi(h)$ for disks confined within a circular boundary or square boundary, as indicated. For the circular boundary, h is defined as the system's diameter normalized by d_s, and for the square boundary system h is defined as the system's side length normalized by d_s. The red (light gray) curves are fits to the data using our model. The image at the lower right is an rcp configuration confined in a circular boundary with $h=21$. Small particles are rendered as green (medium gray) and large particles are rendered as blue (dark gray).

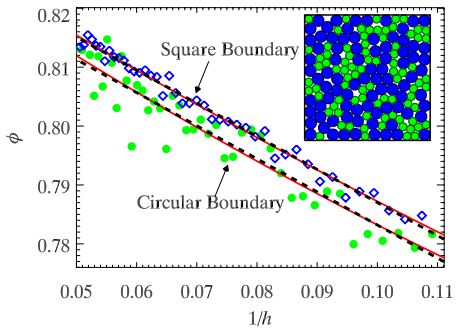

FIG. 14. (Color online) $\phi(1/h)$ for disks confined within a circular boundary or square boundary, as indicated; the data are the same as Fig. 13 along with the definitions of h. The red (light gray) curves are fits to the data using our model. The black dashed lines are linear fits to the data. The image at the upper right is an rcp configuration confined in a square boundary with $h=15.5$. Small particles are rendered as green (medium gray) and large particles are rendered as blue (dark gray).

Note that the data are noisier for two reasons. First, given our algorithm (Sec. II, for samples that are confined in all directions), we can only choose the number of particles we start with; we have no control over the final system size when the particles jam. Due to random fluctuations, we can run the simulations many times with the same number of particles and each time find a different final value for h (and ϕ_{rcp}). This limits our ability to sample enough data at a particular h to reduce the noise and/or look for nonmonotonic effects. Second, there are many fewer particles in these simulations, thus, reducing the statistics. Normally, this could be compensated by increasing the number of simulation runs, but the first problem (lack of precise control over h) frustrates this.

Adapting the model to a circular boundary with diameter h or to a square boundary with side length h, we find that both situations give

$$\phi(h) = \phi_{\mathrm{rcp}} - \frac{2C}{h} + \frac{2C\delta L}{h^2}, \tag{6}$$

where $C=2\delta L(\phi_{\mathrm{rcp}}-\phi_l)$ as before. The data in Fig. 13 are fitted to this model, shown as the red lines. For the circular boundary, the fit gives $\phi_{\mathrm{rcp}}=0.846$, $C=0.371$, and $\delta L=1.51$, and for the square boundary the fit gives $\phi_{\mathrm{rcp}}=0.848$, $C=0.340$, $\delta L=1.14$. These fits give ϕ_{rcp} values close to the ϕ_{rcp} values reported earlier in the paper and C values similar, but slightly different, than that found for one fixed flat boundary. Interestingly, the fits give values of δL commensurate to the λ values previously computed, demonstrating that the boundary produces a thin boundary layer of about 1–2 characteristic particle sizes thick that is primarily responsible for lowering the global packing fraction.

Finally, to demonstrate the quality of the fits we show a plot of $\phi(1/h)$ in Fig. 14. In this figure, the red line is the fit from Eq. (6), while the black dashed line is a linear fit in $1/h$. Both fits are reasonable, and the data are not strong enough to determine which is better. We thus note only that the model suggests we should use the quadratic fit for these cases and that the values of δL obtained are reasonable ones. δL is a third parameter for the fit; fortunately, extending the model to a 3D case, where all directions are confined, would predict a cubic fit but without introducing a fourth parameter.

V. CONCLUSION

In this paper, we have shown how a confining boundary alters the structure of random close packing by investigating simulated rcp configurations confined between rigid walls in 2D and 3D. We find that confinement lowers the packing fraction and induces heterogeneity in particle density, where particles layer in bands near the wall. The structure of the local packing decays from a more ordered packing near the wall to a less ordered packing in the bulk. All measures of local order and local density decay rapidly to their bulk values with characteristic length scales on the order of particle diameters. Thus, the influence of the walls is rapidly forgotten in the interior of the sample, with confinement having the most notable effects when the confining dimension is quite small, perhaps less than 10 particle diameters across.

The results are well fit by a three-parameter model dating back to 1946 [31,32], with our results suggesting that the third parameter (an effective boundary layer thickness) should be a free parameter rather than constrained. To first order, this model suggests that the primary influence of the boundary is quantified by one parameter C, which is the product of a length scale and a volume fraction reduction. This parameter, the boundary packing parameter, thus, quantifies the overall influence of a boundary, near that boundary. Since the model assumes nothing about shape, this model should equally apply to other geometries as well.

These findings have implications for experiments investigating the dynamics of densely packed confined systems (i.e., colloidal suspensions or granular materials). For example, our work shows that for small h the packing fraction has significant variations at small h (most clearly seen in 2D, for example, Fig. 3). For dense particulate suspensions with $\phi<\phi_{\mathrm{rcp}}$, flow is already difficult. By choosing a value of h with a local maximum in $\phi_{\mathrm{rcp}}(h)$, a suspension may be better able to flow, as there will be more free volume available. Likewise, a poor choice of h may lead to poor packing and enhanced clogging. A microfluidic system with a tunable size h may be able to vary the flow properties significantly with small changes in h, but our work implies that control over h needs to be fairly careful to observe these effects. Of course, these effects will be obscured by polydispersity in many systems of practical interest; however, our work certainly has implications for microfluidic flows of these sorts of materials, once the minimum length scales approach the mean particle size.

Our work has additional implications for experiments on confined glasses [50,51,65,67–72]. As mentioned in the introduction, confinement changes the properties of glassy samples, but it is unclear if this is due to finite-size effects or due to interfacial influences from the confining boundaries [73]. Our results show that dense packings have significant structural changes near the flat walls, suggesting that indeed interfacial influences on materials can be quite strong at very short distances, assuming that the structural changes couple

with dynamical behavior. Furthermore, the nonmonotonic behavior of ϕ_{rcp} that we see suggests that experiments studying confined glassy materials could see interesting nonmonotonic effects, if the sample thickness can be carefully controlled.

ACKNOWLEDGMENTS

We thank C. S. O'Hern for helpful conversations. This work was supported by the National Science Foundation under Grant No. DMR-0804174.

[1] A. E. R. Westman and H. R. Hugill, J. Am. Ceram. Soc. **13**, 767 (1930).
[2] H. E. White and S. F. Walton, J. Am. Ceram. Soc. **20**, 155 (1937).
[3] A. H. Boerdijk, Philips Res. Rep. **7**, 303 (1952).
[4] D. P. Haughey and G. S. G. Beveridge, Can. J. Chem. Eng. **47**, 130 (1969).
[5] D. G. Scott, Nature (London) **188**, 908 (1960).
[6] R. M. German, *Particle Packing Characteristics* (Metal Powder Industries Federation, Princeton, NJ, 1989).
[7] S. Torquato, T. M. Truskett, and P. G. Debenedetti, Phys. Rev. Lett. **84**, 2064 (2000).
[8] J. D. Bernal and J. Mason, Nature (London) **188**, 910 (1960).
[9] O. K. Rice, J. Chem. Phys. **12**, 1 (1944).
[10] W. O. Smith, P. D. Foote, and P. F. Busang, Phys. Rev. **34**, 1271 (1929).
[11] S. F. Edwards, *Granular Matter* (Springer-Verlag, Berlin, 1994).
[12] C. Radin, J. Stat. Phys. **131**, 567 (2008).
[13] M. Jerkins, M. Schröter, H. L. Swinney, T. J. Senden, M. Saadatfar, and T. Aste, Phys. Rev. Lett. **101**, 018301 (2008).
[14] R. Pal, Polym. Eng. Sci. **48**, 1250 (2008).
[15] G. Lois, J. Blawzdziewicz, and C. S. O'Hern, Phys. Rev. Lett. **102**, 015702 (2009).
[16] R. Zallen, *Physics of Amorphous Solids* (Wiley, New York, 1983).
[17] C. S. O'Hern, L. E. Silbert, A. J. Liu, and S. R. Nagel, Phys. Rev. E **70**, 043302 (2004).
[18] R. K. Mcgeary, J. Am. Ceram. Soc. **44**, 513 (1961).
[19] A. R. Kansal, S. Torquato, and F. H. Stillinger, J. Chem. Phys. **117**, 8212 (2002).
[20] R. Al-Raoush and M. Alsaleh, Powder Technol. **176**, 47 (2007).
[21] K. Lochmann, L. Oger, and D. Stoyan, Solid State Sci. **8**, 1397 (2006).
[22] H. J. H. Brouwers, Phys. Rev. E **74**, 031309 (2006).
[23] T. Okubo and T. Odagaki, J. Phys.: Condens. Matter **16**, 6651 (2004).
[24] P. Richard, L. Oger, J. P. Troadec, and A. Gervois, Eur. Phys. J. E **6**, 295 (2001).
[25] R. L. Brown and P. G. W. Hawksley, Nature (London) **156**, 421 (1945).
[26] H. S. Leftwich, Nature (London) **156**, 753 (1945).
[27] A. Donev, I. Cisse, D. Sachs, E. A. Variano, F. H. Stillinger, R. Connelly, S. Torquato, and P. M. Chaikin, Science **303**, 990 (2004).
[28] K. Desmond and S. V. Franklin, Phys. Rev. E **73**, 031306 (2006).
[29] Y. Jiao, F. H. Stillinger, and S. Torquato, Phys. Rev. Lett. **100**, 245504 (2008).
[30] P. C. Carman, Trans. Inst. Chem. Eng. **15**, 150 (1937).
[31] L. C. Verman and S. Banerjee, Nature **157**, 584 (1946).
[32] R. L. Brown and P. G. W. Hawksley, Nature (London) **157**, 585 (1946).
[33] G. D. Scott and D. M. Kilgour, J. Phys. D **2**, 863 (1969).
[34] K. Ridgway and K. J. Tarbuck, Br. Chem. Eng. **12**, 384 (1967).
[35] B. R. Aïm and L. P. Goff, Powder Technol. **1**, 281 (1968).
[36] A. G. Dixon, Can. J. Chem. Eng. **66**, 705 (1988).
[37] M. Suzuki, T. Shinmura, K. Iimura, and M. Hirota, Powder Technol. **19**, 183 (2008).
[38] R. Zou, Chem. Eng. Sci. **50**, 1504 (1995).
[39] R. P. Zou and A. B. Yu, Chem. Eng. Sci. **51**, 1177 (1996).
[40] J. W. Landry, G. S. Grest, L. E. Silbert, and S. J. Plimpton, Phys. Rev. E **67**, 041303 (2003).
[41] G. T. Seidler, G. Martinez, L. H. Seeley, K. H. Kim, E. A. Behne, S. Zaranek, B. D. Chapman, S. M. Heald, and D. L. Brewe, Phys. Rev. E **62**, 8175 (2000).
[42] L. Vanel, P. Claudin, J. P. Bouchaud, M. E. Cates, E. Clément, and J. P. Wittmer, Phys. Rev. Lett. **84**, 1439 (2000).
[43] U. Marconi, Physica A **280**, 279 (2000).
[44] P. Claudin and J.-P. Bouchaud, Phys. Rev. Lett. **78**, 231 (1997).
[45] J. Landry, Powder Technol. **139**, 233 (2004).
[46] D. M. Mueth, Phys. Rev. E **67**, 011304 (2003).
[47] J. Ritvanen and P. Jalali, Physica A **387**, 5381 (2008).
[48] L.-W. Teng, P.-S. Tu, and L. I, Phys. Rev. Lett. **90**, 245004 (2003).
[49] C. Murray, MRS Bull. **23**, 33 (1998).
[50] Z. T. Németh and H. Löwen, Phys. Rev. E **59**, 6824 (1999).
[51] M. Alcoutlabi and G. B. McKenna, J. Phys.: Condens. Matter **17**, R461 (2005).
[52] P. Gallo, M. Rovere, and E. Spohr, J. Chem. Phys. **113**, 11324 (2000).
[53] S. Granick, Science **253**, 1374 (1991).
[54] J. R. Henderson, Mol. Phys. **105**, 2345 (2007).
[55] J. Mittal, V. K. Shen, J. R. Errington, and T. M. Truskett, J. Chem. Phys. **127**, 154513 (2007).
[56] J. Mittal, J. R. Errington, and T. M. Truskett, J. Chem. Phys. **126**, 244708 (2007).
[57] J. Mittal, T. M. Truskett, J. R. Errington, and G. Hummer, Phys. Rev. Lett. **100**, 145901 (2008).
[58] I. Cohen, T. G. Mason, and D. A. Weitz, Phys. Rev. Lett. **93**, 046001 (2004).
[59] K. To, P.-Y. Lai, and H. K. Pak, Physica A **315**, 174 (2002).
[60] I. Zuriguel, L. A. Pugnaloni, A. Garcimartín, and D. Maza, Phys. Rev. E **68**, 030301(R) (2003).
[61] S. Redner and S. Datta, Phys. Rev. Lett. **84**, 6018 (2000).
[62] S. B. Fuller, E. J. Wilhelm, and J. M. Jacobson, J. Microelectromech. Syst. **11**, 54 (2002).

[63] K. Sharp and R. Adrian, Microfluid. Nanofluid. **1**, 376 (2005).
[64] G. M. Whitesides, Nature (London) **442**, 368 (2006).
[65] C. R. Nugent, K. V. Edmond, H. N. Patel, and E. R. Weeks, Phys. Rev. Lett. **99**, 025702 (2007).
[66] P. N. Pusey and W. van Megen, Nature (London) **320**, 340 (1986).
[67] D. Morineau, Y. Xia, and C. A. Simionesco, J. Chem. Phys. **117**, 8966 (2002).
[68] J. Schüller, Y. B. Mel'nichenko, R. Richert, and E. W. Fischer, Phys. Rev. Lett. **73**, 2224 (1994).
[69] C. L. Jackson and G. B. McKenna, J. Non-Cryst. Solids **131-133**, 221 (1991).
[70] K. Kim and R. Yamamoto, Phys. Rev. E **61**, R41 (2000).
[71] P. A. Thompson, G. S. Grest, and M. O. Robbins, Phys. Rev. Lett. **68**, 3448 (1992).
[72] P. Scheidler, W. Kob, K. Binder, and G. Parisi, Philos. Mag. A **82**, 283 (2002).
[73] F. He, L. M. Wang, and R. Richert, Eur. Phys. J. Spec. Top. **141**, 3 (2007).
[74] N. Xu, J. Blawzdziewicz, and C. S. O'Hern, Phys. Rev. E **71**, 061306 (2005).
[75] A. S. Clarke and J. D. Wiley, Phys. Rev. B **35**, 7350 (1987).
[76] M. Matsumoto and T. Nishimura, ACM Trans. Model. Comput. Simul. **8**, 3 (1998).
[77] J. Nocedal and S. J. Wright, *Numerical Optimization* (Springer, New York, 1999).
[78] A. Donev, S. Torquato, F. H. Stillinger, and R. Connelly, Phys. Rev. E **70**, 043301 (2004).
[79] A. H. Marcus and S. A. Rice, Phys. Rev. Lett. **77**, 2577 (1996).
[80] P. J. Steinhardt, D. R. Nelson, and M. Ronchetti, Phys. Rev. B **28**, 784 (1983).
[81] U. Gasser, E. R. Weeks, A. Schofield, P. N. Pusey, and D. A. Weitz, Science **292**, 258 (2001).